

Next-to-leading order corrections to Wt production and decay

John Campbell*

*Department of Physics, TH Divison,
CERN, CH-1211 Geneva 23, Switzerland*

Francesco Tramontano[†]

*Dipartimento di Scienze Fisiche, Università di Napoli,
“Federico II” e INFN sezione di Napoli,
Complesso di Monte S. Angelo, Napoli, Italy*

(Dated: November 3, 2018)

Abstract

We present the results of a next-to-leading order calculation of Wt production, including the decays of both the top quark and the W boson. The effects of radiation in the decay of the top quark are also included. The separation of diagrams which appear in the real corrections, into singly- and doubly-resonant contributions, is performed using a b -jet veto which is motivated by the use of the bottom quark distribution function. We find that, for a choice of scale which is suitable for this approach, the QCD corrections are very mild and only change the cross section by up to 10% at the LHC, depending on the severity of the b -jet veto. When further cuts are applied, applicable for a Higgs boson search in the $H \rightarrow WW^*$ channel, we find that the radiative effects greatly decrease the number of background events expected from this process. In addition, the shapes of relevant distributions can be significantly changed at next-to-leading order.

*Electronic address: John.Campbell@cern.ch

[†]Electronic address: Francesco.Tramontano@na.infn.it

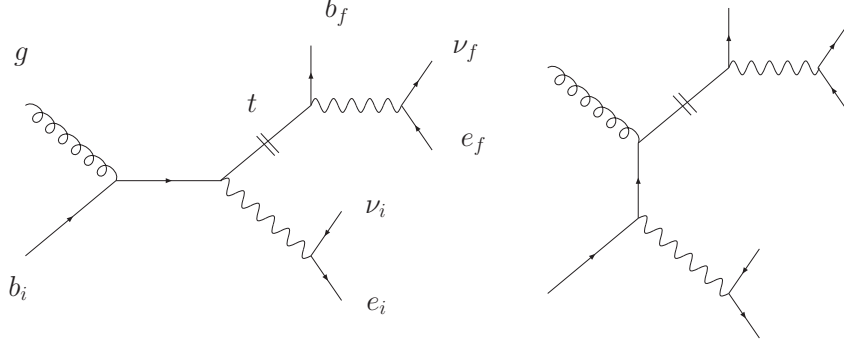


FIG. 1: The two tree level diagrams for the Wt process.

and also use t to represent the momentum of the top quark, so that $t = \nu_f + e_f + b_f$. Both bottom quarks are treated as massless particles in our approach. The two tree-level amplitudes are then given by,

$$\begin{aligned}
 A_- &= \frac{f}{[gb_i]} \left(m_t^2 \langle g e_i \rangle [b_i e_f] - \langle g | t | e_f \rangle \langle e_i \nu_i \rangle [b_i \nu_i] \right), \\
 A_+ &= \frac{f}{\langle g b_i \rangle} \left(\langle b_i | t | e_f \rangle \langle e_i | t | g \rangle - m_t^2 \langle b_i e_i \rangle [g e_f] + 2g \cdot t \langle e_i | t | e_f \rangle \frac{[g \nu_i]}{[b_i \nu_i]} \right), \quad (3)
 \end{aligned}$$

where the overall factor f is,

$$f = \frac{g_s g_w^4 T^a \langle \nu_f b_f \rangle [b_i \nu_i]}{\sqrt{2} g \cdot t W_{prop}^+ W_{prop}^- t_{prop}}. \quad (4)$$

In these formulae $P_{prop} = P^2 - M_P^2 + iM_P \Gamma_P$, T^a represents one of the eight $SU(3)$ color generators and the spinor products with massless four-momenta p_i and p_j are defined as usual:

$$\langle p_i p_j \rangle = \langle p_i - | p_j + \rangle, \quad (5)$$

$$[p_i p_j] = \langle p_i + | p_j - \rangle, \quad (6)$$

$$\langle p_i | p_k | p_j \rangle = \langle p_i - | \not{p}_k | p_j - \rangle. \quad (7)$$

As explained above, the virtual corrections to this process can be divided into production stage corrections (represented in Fig. 2) and decay stage ones (shown in Fig. 3). The same division applies to the real corrections, which are depicted in Figs. 4 and 5 respectively. By producing the top quark strictly on shell we are assured that the diagrams in Figs. 4 and 5 are separately gauge invariant.

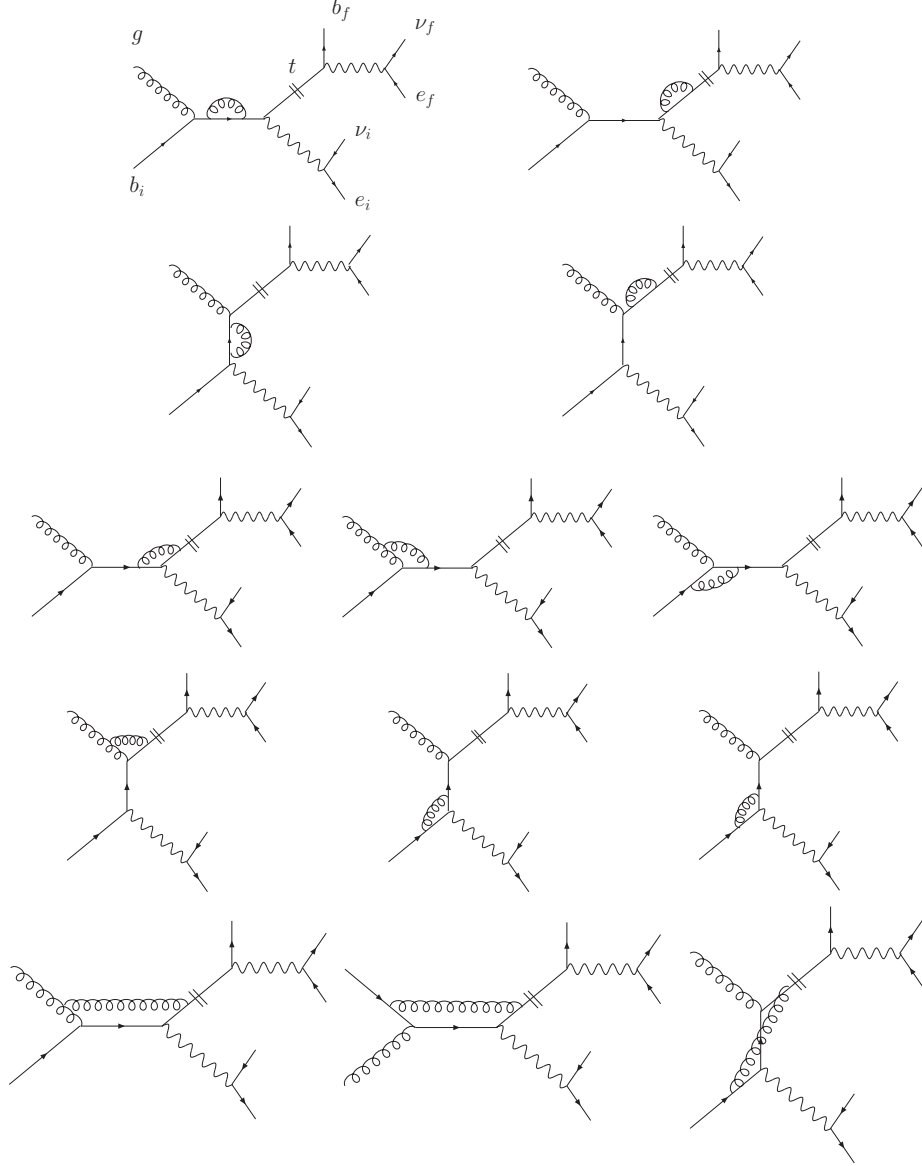


FIG. 2: One loop diagrams representing virtual corrections in the production stage.

The cancellation of the soft and collinear divergences between real and virtual contributions has been implemented through the subtraction method [11]. In particular, for the contribution from real radiation in the production stage we have adopted an extension of the dipole subtraction scheme [12, 13] which handles the case of massive quarks in the final state [14]. We have used a generalization of this method, where one can use a tuneable parameter in order to have better control over the size of the subtraction. Further details and formulae are contained in Ref. [10] and Appendix A. For the case of real radiation in the decay we have used a further extension of this method, as in Ref. [10], which ensures

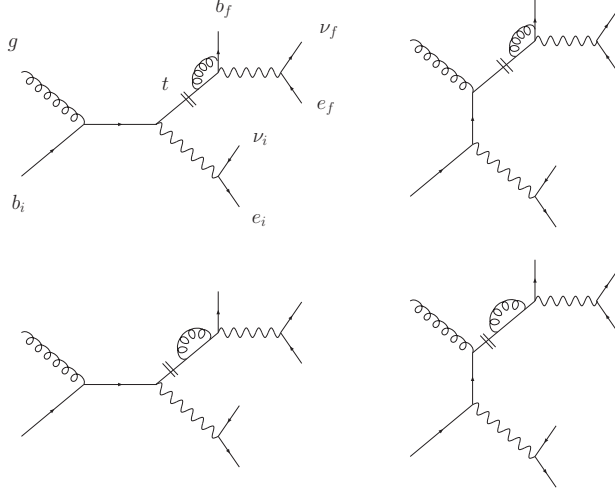


FIG. 3: One loop diagrams contributing to the calculation of virtual radiation in the decay stage.

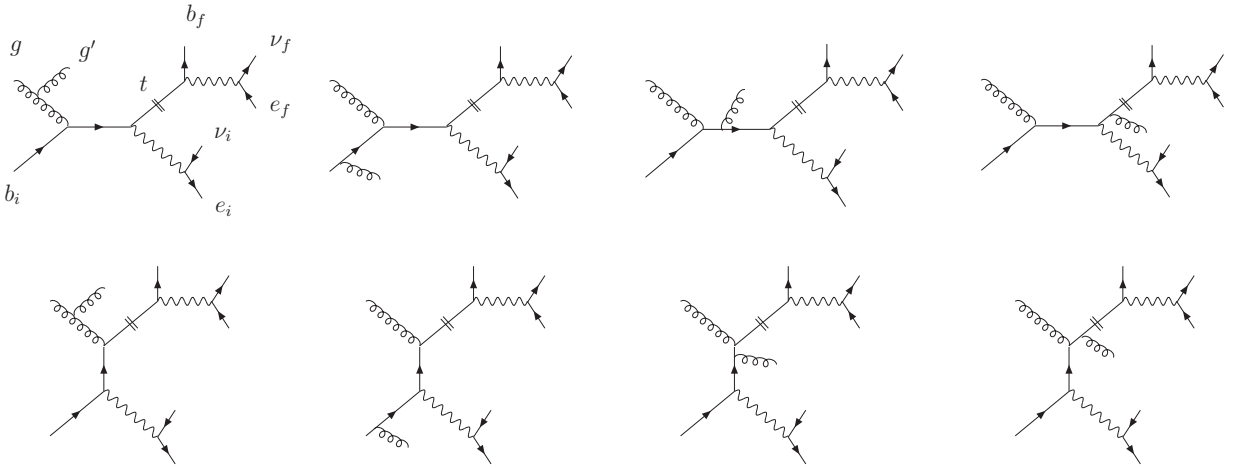


FIG. 4: Diagrams representing the emission of real radiation in the production stage. In the calculation, the additional gluon must also be crossed into the initial state and diagrams containing two quark lines (not shown) are also included.

that the top quark and the W boson remain on-shell when the subtraction is performed.

The virtual corrections in the decay stage amount to the study of the decay of an on-shell top quark. These amplitudes have been known for a long time [15, 16] and we do not report them here. To evaluate the contribution of the virtual radiation in the production stage (Fig. 2) we start from the amplitudes where the top quark is produced on-shell without decaying and calculate amplitudes for the two polarization states of the top quark. This

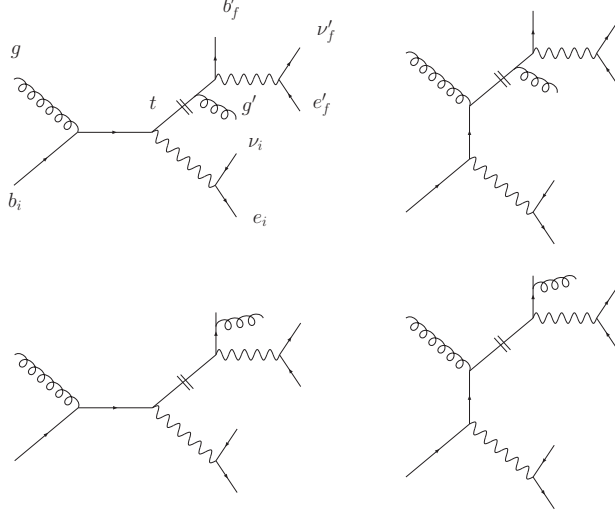


FIG. 5: Diagrams contributing to real radiation in the decay of the top quark.

is achieved by writing the spinors in terms of an auxiliary massless four-vector t_0 in the following way:

$$\begin{aligned}
 u(t)_\uparrow &= \frac{(\not{t} + m_t)}{[t_0 g]} |g, -1\rangle, & \bar{u}(t)_\uparrow &= \langle g, -1| \frac{(\not{t} + m_t)}{\langle g t_0 \rangle}, \\
 u(t)_\downarrow &= \frac{(\not{t} + m_t)}{\langle t_0 g \rangle} |g, +1\rangle, & \bar{u}(t)_\downarrow &= \langle g, +1| \frac{(\not{t} + m_t)}{[g t_0]}.
 \end{aligned} \tag{8}$$

The vector t_0 is constructed by forming a linear combination of t and g ,

$$t_0^\mu = t^\mu - \frac{m_t^2}{2t \cdot g} g^\mu. \tag{9}$$

The full result, where the decay of the top quark is included, can then be obtained by combining these amplitudes with the ones for the decay $t \rightarrow Wb$, calculated in the same way. This is possible since the intermediate top quark propagator is recovered via the identity,

$$u(t)_\uparrow \bar{u}(t)_\uparrow + u(t)_\downarrow \bar{u}(t)_\downarrow = \not{t} + m_t. \tag{10}$$

Performing the calculation in this factorized way has a number of advantages. First, useful consistency checks can be performed using the amplitudes without the top quark decay. Second, by replacing the top quark mass appropriately, these amplitudes can be used to study other processes where this decay is not relevant.

The diagrams of Fig. 2 have been written and algebraically manipulated using FORM, after we have used the background field gauge to contain the number of terms generated

by the three gluon vertex. We deal with infrared and ultraviolet singularities by using dimensional regularization in the four dimensional helicity scheme and use the method of Ref. [17] to write the amplitudes in terms of traces. The appearance of γ_5 in the weak vertex is then handled by cyclically rotating these traces so that γ_5 appears at the beginning of each trace, before performing the contraction of Lorentz indices. Using this prescription we have checked that the Ward identity for the weak current is satisfied exactly and no additional counter terms are required.

Finally, we are left with box vector integrals and triangle rank 2 tensor integrals. Using Passarino-Veltman n -dimensional decomposition, we obtain a result in terms of scalar integrals. Due to the nature of our approach, other spurious divergences are still present at this stage. Individual terms in the result appear to be divergent as factors in the denominator approach zero. However, in this limit, a combination of such apparently-singular terms is finite. By collecting all such terms over a common denominator, one can identify new functions that are well-behaved in these limits. These are combinations of rational and logarithmic functions, as in Ref. [18]. Following this procedure, we are able to refine our first result considerably. To show the level of simplification that we have reached, one of the amplitudes is reported in Appendix B. The others are slightly larger in size and we do not reproduce them here. They will be available, together with the rest of our calculation, as part of the next release of the Monte Carlo program MCFM.

III. SEPARATION OF Wt AND $t\bar{t}$ DIAGRAMS

When calculating the real radiation corrections, all appropriate crossings of the diagrams shown in Fig. 4 should be included. Some of the crossings, in which the additional parton is a \bar{b} quark in the final state, are particularly problematic. These diagrams are shown in Fig. 6 and involve gluon-gluon and same flavour quark-antiquark initial states, which are important at the LHC and Tevatron respectively. All these diagrams produce a final state consisting of a W^- , an on-shell top quark and a \bar{b} quark. However, the diagrams in panel (b) contain a resonant \bar{t} propagator and represent the production of a $t\bar{t}$ pair with the subsequent decay of the \bar{t} into the W^- and \bar{b} quark. As such, the contribution from these diagrams when integrated over the total available phase space can be much larger than the lowest order Wt cross section (an order of magnitude at the LHC). In order to disentangle

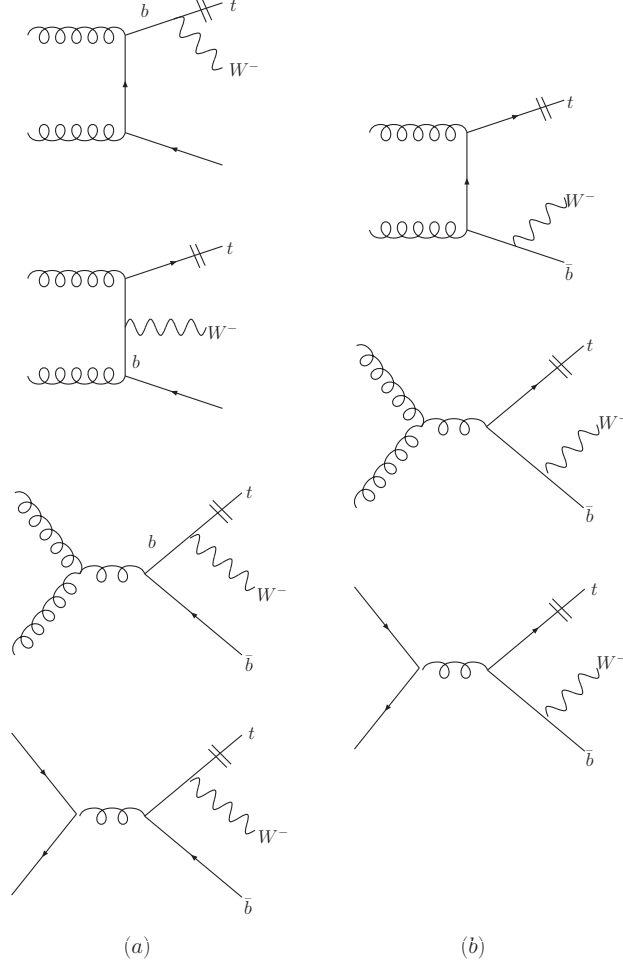


FIG. 6: Real corrections to W^-t production which involve an additional \bar{b} quark. The double bars indicate the on-shell top quark which subsequently decays into W^+b . Diagrams obtained by interchanging two gluons are not shown. The 3 representative diagrams in the right panel (b) contain a resonant \bar{t} propagator, while those on the left (a) do not.

these two processes, two methods have been outlined in the literature.

The first involves making a cut on the invariant mass of the $W^-\bar{b}$ system to prevent the \bar{t} propagator from becoming resonant [5]. The second method instead subtracts the contribution from the resonant diagrams so that no on-shell piece remains [6]. A comparison of these two approaches [7] shows that the methods yield the same total cross section when a mass window of $15\Gamma_t \approx 25$ GeV either side of the top mass is chosen. However, these methods do not lend themselves to a Monte Carlo implementation where one wishes to study distributions of final state particles as well as total cross sections. Therefore we shall

adopt neither of these prescriptions but instead follow a procedure motivated by our use of the bottom quark PDF.

In the b -PDF approach, the b quark distribution function is derived perturbatively from a collinear $g \rightarrow b\bar{b}$ splitting that occurs in the initial state. It implicitly includes all splittings up to a p_T of the \bar{b} -quark equal to the factorization scale, μ_F . This means that the contribution from the corresponding $gg \rightarrow Wtb$ diagrams (contained in panel (a) of Fig. 6) has already been included in the lowest order calculation. Therefore the net contribution from these diagrams, including appropriate counter-terms and integrating over all \bar{b} quark transverse momenta up to μ_F , should be approximately zero. For a suitable choice of μ_F we have checked that this is indeed the case. The choice of μ_F is made such that the collinear approximation used in deriving the b -PDF is accurate, which for this process implies that $\mu_F \lesssim (m_W + m_t)/4 \approx 65$ GeV [39].

There is also a contribution from the diagrams in panel (b) of Fig. 6 when the p_T of the \bar{b} quark is small, $p_T^{\bar{b}} < \mu_F$. However, these diagrams simply represent the doubly-resonant $t\bar{t}$ production process which is currently known up to NLO [40]. Therefore it is preferable to separate this contribution from the ‘genuine’ NLO corrections to the Wt process. As we shall show later, although the contribution from the $t\bar{t}$ diagrams in this region of phase space is rather small in relation to the total cross section, it is still competitive with the Wt result. This suppression means that the interference effects between the two sets of diagrams is very small when using a b -jet veto, in contrast to the case when p_T^b is unconstrained [7].

When a \bar{b} quark is observed with a p_T above μ_F then our description of the final state is a lowest order one. The contribution from the doubly-resonant diagrams dominates and, as above, a better prediction would be obtained by using the $t\bar{t}$ process. Alternatively, one could use a calculation including all the diagrams for $gg \rightarrow tWb$, including the $t \rightarrow bW \rightarrow b\ell\nu$ decay (retaining the b quark mass) and also finite width effects [21]. However, currently this study would be limited to leading order in α_s only.

To summarize, we shall perform our calculation of the Wt process by applying a veto on the p_T of the additional b quark that appears at next-to-leading order. This aids the separation of this process from doubly-resonant $t\bar{t}$ production. When applying this veto, one should choose the factorization scale equal to (or at least of the same order as) the maximum p_T of the b quark that is allowed, $p_T^{\bar{b} \text{ veto}}$. This choice respects the approximations that were originally used to define the b quark PDF. For $\mu_F \neq p_T^{\bar{b} \text{ veto}}$ and for less inclusive

quantities, the contribution from the $gg \rightarrow Wtb$ diagrams is calculated by simply omitting the doubly-resonant diagrams [41]. The result for this piece remains at the level of a few percent of the lowest order cross section.

IV. RESULTS

Before discussing the effect of including radiation in the decay of the top quark, we will first consider just the Wt total cross section in order to discuss some features of our approach and to compare our results with those available in the literature.

A. Comparison with no top quark decay

The NLO corrections to the total Wt cross section, where no decay of the top quark is included, were previously presented in Ref. [9]. For the sake of comparison, in this section we will adopt the parameters therein as closely as possible. In particular, we choose $m_t = 175$ GeV and the CTEQ5 set of parton distribution functions [42]. The other electroweak parameters that enter our calculation are chosen to be,

$$M_W = 80.419 \text{ GeV}, \quad g_W^2 = 0.4267. \quad (11)$$

We perform our comparison at the LHC and examine the dependence of our results on the common renormalization and factorization scale μ . As we have already argued, the b -PDF approach is most well-motivated when choosing a value of μ less than about 65 GeV. However, such a value is much smaller than the more typical choice, $\mu = m_t + m_W$ which is the central value chosen in Ref. [9]. Therefore, for the sake of illustration, we choose to study the scale dependence over a large range from $\mu = 25$ GeV up to $\mu = m_t + m_W = 255$ GeV. As we have discussed above, we limit the p_T of the b quark that appears at next-to-leading order to have a maximum value $p_T^{\bar{b} \text{ veto}}$, which we choose here to be 50 GeV.

Our results at LO and NLO are shown in Fig. 7. We see that the dependence of the lowest order curve on a common scale choice is already remarkably small. At next-to-leading order we see that this is improved still further, with the cross section varying by about 3% over the range of scales shown in the figure.

Comparing with Zhu [9], we find a number of differences. Even at lowest order our result for $\mu = m_t + m_W$ is higher and furthermore, the dependence of the result on this scale

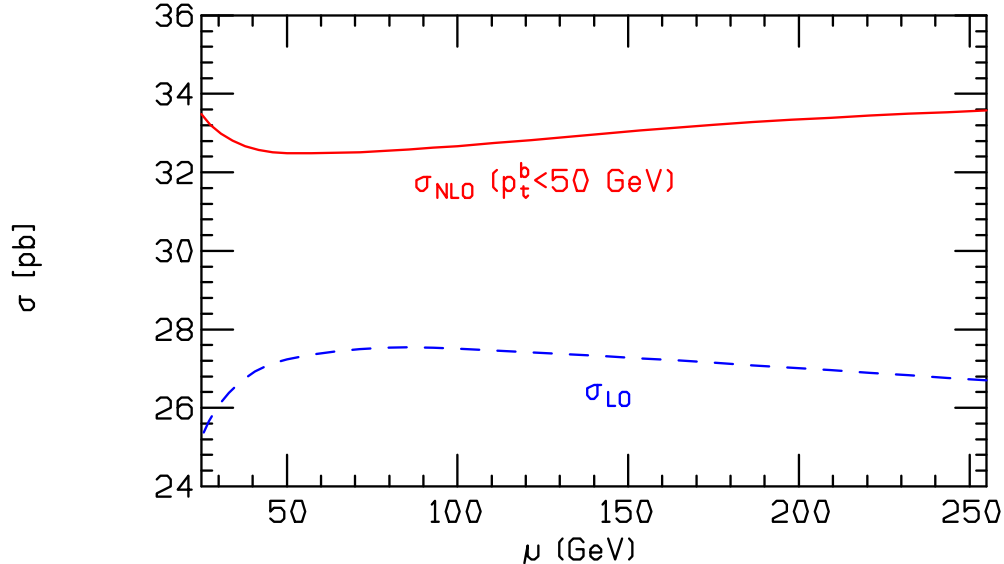


FIG. 7: Scale dependence of the cross sections for W^-t production at the LHC for $m_t = 175$ GeV. The branching ratios for the decay of the top quark and the W 's are not included. Cross sections are evaluated with CTEQ5L1 ($\alpha_s(M_Z) = 0.127$) and CTEQ5M1 ($\alpha_s(M_Z) = 0.118$) PDFs [22]. We choose a single common renormalization and factorization scale, μ . The lowest order cross section is the dashed curve, whilst the NLO one – calculated with $p_T^{\bar{b} \text{ veto}} = 50$ GeV – is solid.

appears less mild (c.f. Fig. 2 of Ref. [9]). However, we have checked the lowest order results of our program against those obtained with MadEvent [23] and found good agreement. At next-to-leading order we also find a slightly different result, lower and with a stronger dependence on the scale. In this case, we expect some discrepancy due to our different method of handling the $gg \rightarrow Wtb$ contribution. We note that the combination of the \bar{b} -jet veto and our preferred choice of a much smaller scale, leads to a next-to-leading order cross section that is about 15% smaller than that found by Zhu. In addition, the K -factor, defined as the ratio of NLO and LO cross sections, is much smaller and in the range 1.2–1.3 depending on the scale choice.

Finally, we consider the dependence of our result on the choice for $p_T^{\bar{b} \text{ veto}}$. In Fig. 8 we show the scale dependence for three different choices of the veto threshold. We have concentrated on the region of smaller scales and varied the common scales by a factor of two about the central value $\mu_0 = p_T^{\bar{b} \text{ veto}}$. One sees that, within this window, the scale dependence of the next-to-leading order calculation is again somewhat smaller than that found at LO

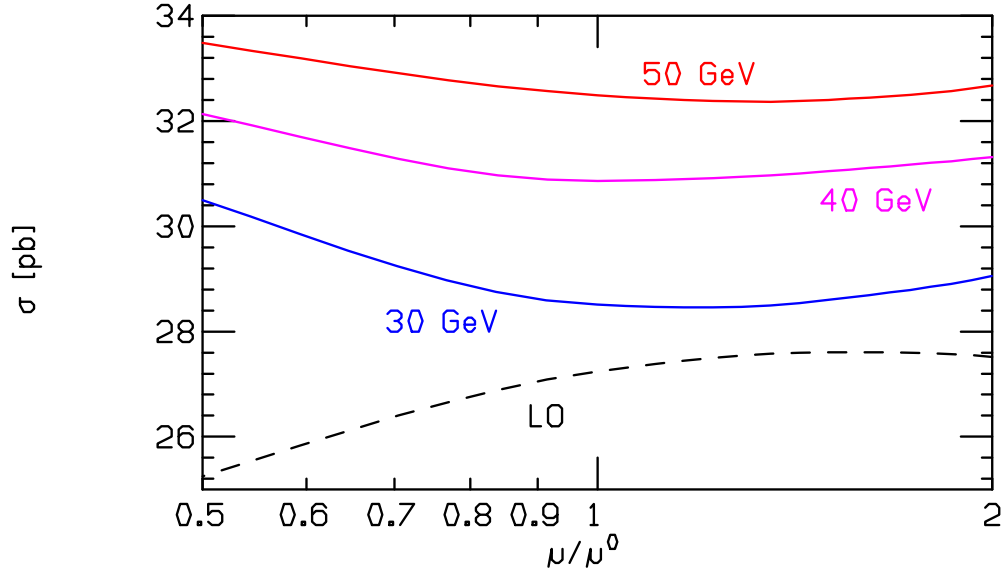


FIG. 8: Scale dependence of the cross sections for W^-t production at the LHC, for three different choices of $p_T^{\bar{b} \text{ veto}} = \mu_0$. From bottom to top, the solid curves represent values of 30, 40 and 50 GeV. The lowest order dashed curve (calculated with $\mu_0 = 50$ GeV) is also shown for reference.

and improves as the veto threshold is raised. Compared to a threshold of 50 GeV, the cross section decreases by about 15% when lowering the veto to 30 GeV. This substantially reduces the effect of the next-to-leading order corrections on the cross section, leaving a K -factor close to unity for our central scale choice.

B. Updated results and radiation in the decay

First, we repeat the calculation of the total Wt cross section, but using the most recent determination of the top quark mass [24], which yields $m_t = 178$ GeV. We also use recent PDF sets from the MRST and CTEQ groups.

Our predictions for the Tevatron and the LHC are shown in Table I, where we have used $p_T^{\bar{b} \text{ veto}} = 50$ GeV and factorization and renormalization scales also equal to this value. It is clear from the quoted cross sections that this process is of little phenomenological relevance at the Fermilab collider, although we include the result here for completeness. The NLO corrections at the Tevatron increase the cross section by a factor of 1.35 when using the CTEQ PDF set, but decrease it by a little under 10% for the MRST parametrization. The

TABLE I: LO and NLO cross sections for single top-quark production in association with a W^- at the Tevatron and LHC, for $m_t = 178$ GeV. The branching ratios for the decays of the top quark and the W^- are not included. Cross sections are evaluated with CTEQ6L1 ($\alpha_s(M_Z) = 0.130$) and CTEQ6M ($\alpha_s(M_Z) = 0.118$) PDFs [25] and also with the MRST2002 NLO PDF set ($\alpha_s(M_Z) = 0.1197$) [26]. The renormalization and factorization scales are set to the \bar{b} jet veto threshold of 50 GeV. The errors represent Monte Carlo statistics only.

Collider, \sqrt{s}	PDF	σ_{LO} [pb]	σ_{NLO} [pb]
$p\bar{p}$, 1.96 TeV	CTEQ6	0.04796	0.06458 ± 0.0001
$p\bar{p}$, 1.96 TeV	MRST2002	0.08083	0.07414 ± 0.0001
pp , 14 TeV	CTEQ6	29.41	32.10 ± 0.03
pp , 14 TeV	MRST2002	31.08	34.49 ± 0.03

NLO results still differ by about 15%, reflecting the considerable uncertainty in the gluon distribution at large x . At the LHC the effect of the NLO corrections is much smaller, increasing the cross section by about 10% in both cases, and the predictions from the two PDF sets show much better agreement.

We now turn to a fuller description of the final state, where all the leptonic decays of the top quark and the W bosons are included, as in Eq. (1). The decays are included using Breit-Wigner propagators with widths,

$$\Gamma_W = 2.06 \text{ GeV}, \quad \Gamma_t^{LO} = 1.651 \text{ GeV}, \quad (12)$$

and we now investigate the effects of the inclusion of gluon radiation in the decay of the top quark. Although the inclusion of this radiation should not change the total cross section, a difference is expected when working at a fixed order of perturbation theory. Our results are summarized in Table II. We have used the CTEQ6M PDF set for all the cross sections in this table, so that the effect of including radiation in the decay can be understood more easily. When including radiation in the decay, the total cross section should change by an amount that is formally of higher order in α_S and is given by [10],

$$\sigma_{B_{t \rightarrow b\nu e+X}} - \sigma_{B_{t \rightarrow b\nu e}} = \left(\frac{\Gamma_t^{LO}}{\Gamma_t^{NLO}} - 1 \right) (\sigma_{B_{t \rightarrow b\nu e}} - \sigma_0 B_{t \rightarrow b\nu e}). \quad (13)$$

TABLE II: Comparison of LO and NLO cross sections for W^-t production at the Tevatron and LHC, with leptonic decays of both the W^- and the top quark. The NLO calculation is performed both without including QCD effects in the decay ($\sigma B_{t \rightarrow b\nu e}$) and also when it is included ($\sigma B_{t \rightarrow b\nu e+X}$). The top quark mass is $m_t = 178$ GeV and cross sections are evaluated using the CTEQ6M PDF set with all scales equal to 50 GeV. The errors represent Monte Carlo statistics only. Note that the values of Γ_t at LO and NLO are 1.651 GeV and 1.480 GeV respectively and the branching ratio of the W into leptons is $\text{Br}(W \rightarrow e\nu) = 0.1105$.

Collider, \sqrt{s}	$\sigma_0 B_{t \rightarrow b\nu e}$ [fb]	$\sigma B_{t \rightarrow b\nu e}$ [fb]	$\sigma B_{t \rightarrow b\nu e+X}$ [fb]
$p\bar{p}$, 1.96 TeV	0.8564 ± 0.0006	0.7887 ± 0.0005	0.7806 ± 0.0005
pp , 14 TeV	356.9 ± 0.2	391.7 ± 0.3	395.7 ± 0.3

The results shown in the table agree with this expectation. Since, in our approach, the effect of the NLO corrections in the production is fairly small, the numerical difference is only 1% at both colliders.

We conclude this section with a more detailed presentation of the scale dependence of our calculation when using the updated parameters and PDF set. Anticipating the study of the following section, we also choose a lower value for the \bar{b} jet veto in the next-to-leading order calculation, $p_T^{\bar{b} \text{ veto}} = 30$ GeV. This results in the scale dependence shown in Fig. 9, where the cross sections at each choice of scale are expressed as a ratio with the central result at $\mu_0 = p_T^{\bar{b} \text{ veto}}$ and we vary the scales by a factor of two about μ_0 . We also show the curves obtained when varying the renormalization and factorization scales separately. One sees that the relatively small scale dependence at lowest order is the result of a large cancellation between the dependence on the factorization and renormalization scales individually. In contrast, the dependence on these scales at next-to-leading order, either on their own or when varied together, is small – less than 10% over this range. We also note that, for this choice of parameters and veto, the next-to-leading order corrections do not alter the tree level cross section, which remains at 346 fb.

In previous studies [30, 31] two top backgrounds have been considered using Pythia [32]. These are resonant $t\bar{t}$ production and Wt production, the process that we consider here. As we have discussed previously, these two processes become entangled at NLO. We will separate them according to the procedure that we outlined in Section III. Therefore, in addition to our NLO calculation of the Wt process, we will also consider the contribution from resonant $t\bar{t}$ production, with the appropriate top quark decays.

Since the signal process contains no jets at lowest order, it is efficient to impose a veto on all jet activity to reduce the size of these backgrounds. Our application of a cut on the transverse momentum of the \bar{b} jet in the Wt process fits naturally into this procedure. We simply extend our veto to disallow all contributions with any jet observed above the veto threshold. We note that there is a slight mismatch due to the fact that our theoretically-motivated veto applies at all rapidity values whilst the experimental approach only vetoes a jet up to a few units of rapidity. However, we do not expect this to greatly affect our results.

For our parton-level study we adopt a minimal set of cuts and examine the effect of the NLO corrections on a selection of observables that are typically used in more detailed experimental studies [27, 29, 30, 31]. Our basic cuts represent the finite acceptance limits of the detectors at the LHC,

$$p_T(\text{lepton}) > 20 \text{ GeV}, \quad |\eta(\text{lepton})| < 2.5, \quad (15)$$

applied to both of the leptons produced in the W decays, with the missing transverse momentum also constrained by,

$$p_T(\text{missing}) > 30 \text{ GeV}. \quad (16)$$

The final cut that we apply is the jet veto, after potential jets have been clustered according to the k_T algorithm with a jet separation parameter $\Delta R = 1.0$. Events are not included if any jet is observed with,

$$p_T(\text{jet}) > 30 \text{ GeV}, \quad |\eta(\text{jet})| < 3. \quad (17)$$

We note that, in addition to excluding additional radiation at next-to-leading order, this veto also applies to the b jet that is produced in the top quark decay. This results in a substantial decrease in cross section compared to the totally inclusive case.

To exploit the spin correlation between the leptons in the signal events [33], one can make quite stringent cuts on the opening angle between the leptons in the transverse plane, $\Delta\phi_{\ell\ell}$.

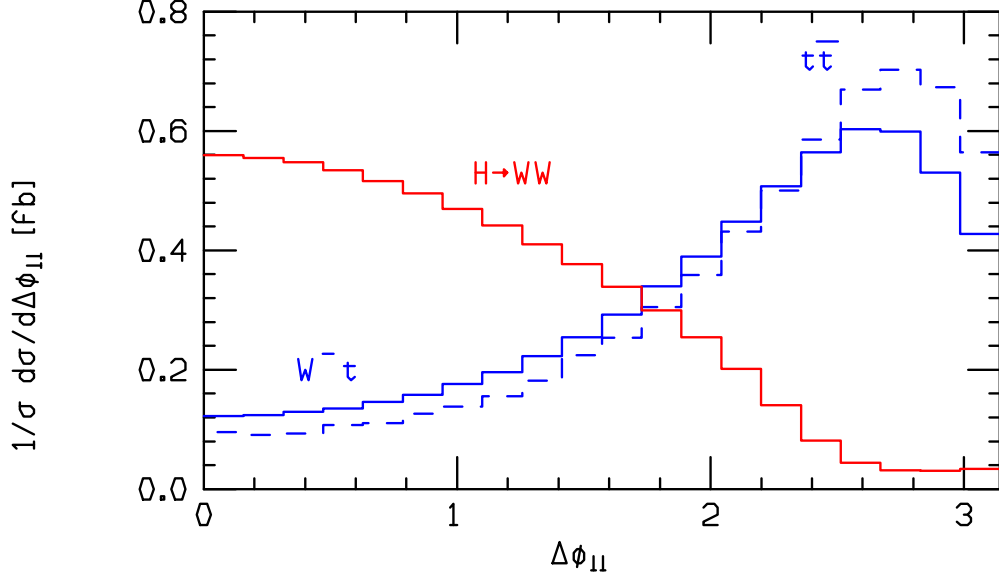


FIG. 10: The distribution of the opening angle between the leptons in the transverse plane, for the signal and the two background processes considered here. All curves are lowest order predictions and are normalized to unity. The signal calculation uses a Higgs mass of 155 GeV and the backgrounds are W^-t (solid) and $t\bar{t}$ (dashed).

This is illustrated in Fig. 10, where we show the shapes of the lowest order predictions for the Higgs signal and the two top backgrounds, Wt and $t\bar{t}$. Signal events predominantly contain leptons with a small opening angle between them, whereas both backgrounds tend to produce leptons that are almost back-to-back in the transverse plane.

We now examine the extent to which this is changed in our NLO calculation of the Wt background, with our results shown in Fig. 11. The effect of the NLO corrections is to change the shape of the distribution considerably when these cuts are applied. The peak at large $\Delta\phi_{\ell\ell}$ is shifted to a smaller value and becomes much less pronounced. This could have quite a large impact on a strategy in which this background is measured using events at large $\Delta\phi_{\ell\ell}$ and then extrapolated via the theoretical shape to the Higgs signal region. One also sees that the shape is changed again when including the effects of radiation in the top quark decay, with the peak being sharpened once more, although the effect is fairly minor.

One can also imagine constructing the transverse mass of the putative Higgs boson (m_T) from the transverse momenta of the dilepton system and the missing p_T ,

$$m_T = \sqrt{2p_T^{\ell\ell} p_T^{\text{miss}} (1 - \cos(\Delta\phi))}, \quad (18)$$

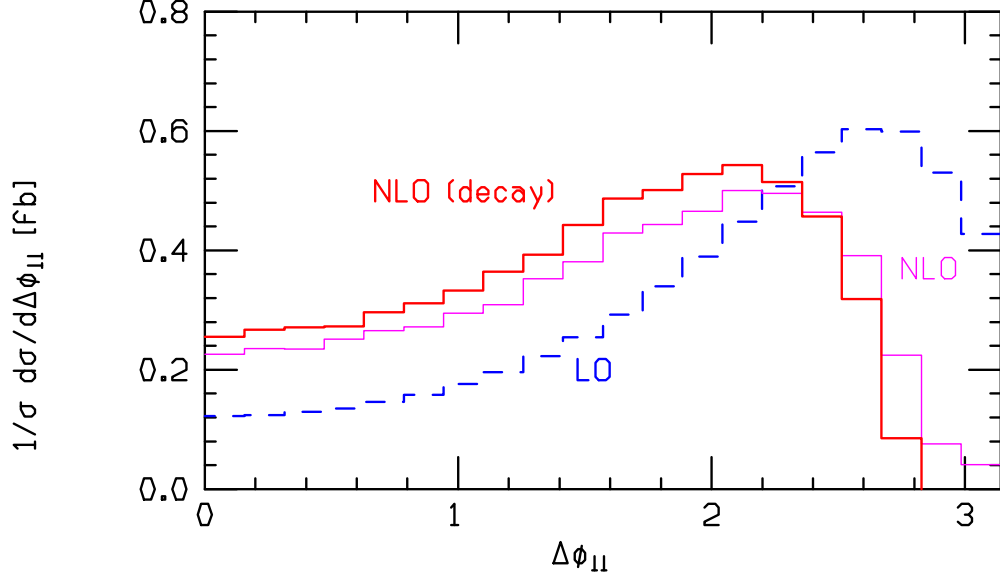


FIG. 11: The distribution of the opening angle between the leptons in the transverse plane for W^-t events at the LHC, calculated at LO (dashed) and NLO (solid) for the LHC. The NLO curves are labelled according to whether or not they include the effect of radiation in the decay. All the rates are normalized to unity.

where $\Delta\phi$ is the angle between the two vectors in the transverse plane. Cutting in a suitable mass window can further help to reduce the backgrounds for only a small loss in signal. The impact of our next-to-leading order calculation on this distribution is illustrated in Fig. 12. In this figure we have only shown the result when including radiation in the decay but note that this distribution changes little when it is excluded. One can see that the shape of this distribution is relatively unchanged at NLO, although more events are produced at high values of M_T , beyond the peak of the distribution, than at LO.

Finally, to give some idea of the effect of the NLO corrections on the number of events that should be observed in this channel, in Table III we show the cross sections that we find for the Wt and $t\bar{t}$ processes. The W 's decay into electrons only and for the Wt process, both W^-t and $W^+\bar{t}$ are included. Results are shown at LO, NLO and at NLO when including radiation in the top quark decay. For the $t\bar{t}$ process, the lowest order diagrams of Fig. 6 (b) are calculated. As an approximation to the NLO result, a K -factor is applied from the NLO calculation involving no top quark decay. In order to match the study more closely, we have used a K -factor obtained when applying the jet veto of Eq. (17). Using the common scales

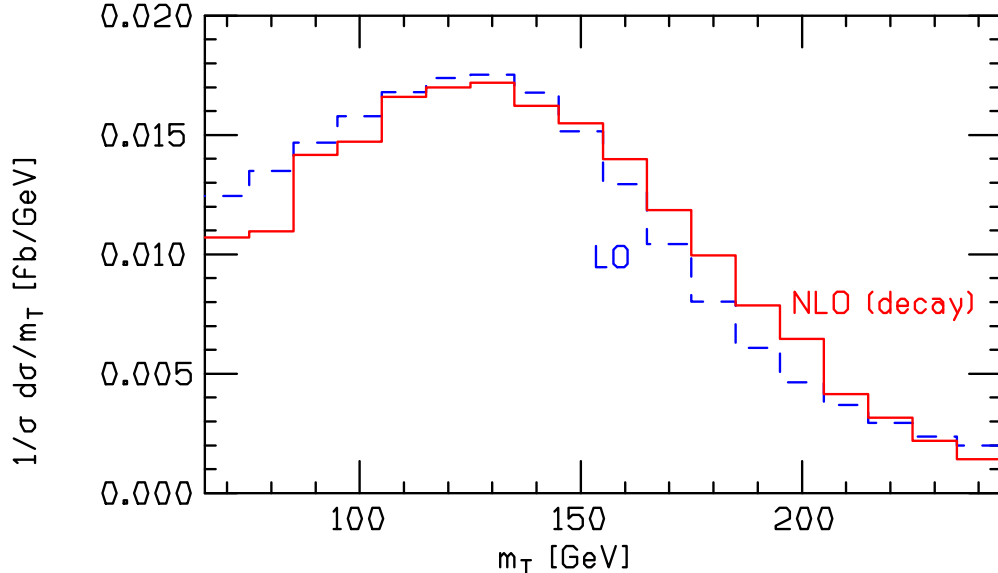


FIG. 12: The distribution of the transverse mass for W^-t events at the LHC, calculated at LO (dashed) and NLO (solid) for the LHC. The NLO result includes the effect of radiation in the decay. The rates are normalized to unity.

$\mu_R = \mu_F = m_t$, we find that this factor is $\mathcal{K} = 0.7$.

The cross sections shown in Table III are evaluated using three different sets of cuts. The first column uses just the basic set of cuts (Eqs. (15)–(17)), then the other two columns represent extensions of these cuts that might be used in the search for a Higgs boson of given mass. Both the further sets also impose,

$$\begin{aligned} \Delta\phi_{\ell\ell} &< \pi/4, \\ m_{\ell\ell} &< 35 \text{ GeV}, \end{aligned} \tag{19}$$

to select the Higgs signal region. In addition we have used a cut on the reconstructed transverse mass around the Jacobian peak of the putative Higgs mass. In the first case, the cut is constructed for a Higgs mass of 155 GeV, by constraining $125 < m_T < 155$ GeV. The second set requires that $140 < m_T < 180$ GeV and is aimed at a search for a 180 GeV Higgs.

One sees that the effect of the NLO corrections in this region of phase space is significantly different from the inclusive case. The cross section is decreased substantially, with a K -factor (for the calculation including radiation in the decay) of approximately 0.6 when applying the Higgs search cuts. We also see that the contributions from the two top quark processes

TABLE III: Comparison of LO and NLO cross sections for top quark backgrounds in an intermediate mass Higgs search at the LHC. Results are shown in femtobarns for $(W^-t + W^+\bar{t})$ and $t\bar{t}$ production, with leptonic decays of both the W and the top quark. Three sets of cuts are considered, which are described in detail in the text. The NLO Wt calculation is performed both without including QCD effects in the decay ($\sigma B_{t \rightarrow b\nu e}$) and also when it is included ($\sigma B_{t \rightarrow b\nu e+X}$).

	basic	$m_H = 155$ GeV	$m_H = 180$ GeV
Wt process			
$\sigma_0 B_{t \rightarrow b\nu e}$ [fb]	40.08	0.80	0.80
$\sigma B_{t \rightarrow b\nu e}$ [fb]	13.14	0.38	0.43
$\sigma B_{t \rightarrow b\nu e+X}$ [fb]	13.85	0.46	0.51
$t\bar{t}$ process			
$\sigma_{LO} \times \mathcal{K}$ [fb]	30.52	0.42	0.43

are comparable when calculated in this way.

VI. CONCLUSIONS

At the LHC, the top quark will be readily produced in association with a W boson. In this paper we have performed a next-to-leading order calculation of this process, including both the subsequent leptonic decays $W^- \rightarrow e^- \bar{\nu}$ and $t \rightarrow \nu e^+ b$, as well as the emission of real radiation in the top decay.

For total inclusive cross sections, where the top quark and W^- boson do not decay, comparison with previous calculations is possible and we find results which are broadly similar. However, due to the presence of doubly-resonant $t\bar{t}$ diagrams at NLO – which are handled differently in our calculation – we do not find exact agreement. Our method maintains the consistency of the b -PDF approach and requires the simultaneous use of a relatively low factorization scale $\mu_F \sim (m_t + m_W)/4$ and a veto on \bar{b} quarks with a transverse momentum larger than this value of μ_F .

With this approach, we find that the NLO corrections to the inclusive rate at the Tevatron can be large, but the process remains phenomenologically irrelevant there. At the LHC

the corrections are smaller and can either increase or decrease the cross section by 10%, depending on the \bar{b} quark veto that is chosen. We also performed an analysis of this process as a background to Higgs production at the LHC, where quite a severe veto on all jet activity is applied. We find that the shape of the $\Delta\phi_{\ell\ell}$ distribution – crucial to the estimation of this background – is significantly changed. However the cross section for this process can be reduced by as much as 40% in the Higgs signal region.

Our predictions are based on a number of approximations. Firstly, the mass of the b quark is set to zero throughout and the top quark is kept on its mass shell. The inclusion of the b -mass in the top quark decay and implementation of a Breit-Wigner distribution for the top quark can be studied in the lowest order calculation. Neither of these significantly alters the total cross section or the shapes of the distributions which we have examined. Effects due to the interference between radiation in the production and decay stages are estimated to be similarly small, of order $\alpha_s\Gamma_t/m_t$. Lastly, our predictions are performed at parton-level only and lack any modelling of hadronization and showering. This is particularly relevant to our phenomenological analysis, where the application of a jet veto at relatively low transverse momenta (compared to the top quark mass) increases the sensitivity to soft-gluon effects. Nevertheless, we hope that our results can provide a starting point for further investigation of the Wt process at next-to-leading order accuracy.

Acknowledgments

We thank K. Ellis for collaboration in the early stages of this work and we would like to acknowledge many helpful discussions with F. Maltoni and S. Willenbrock.

APPENDIX A: INTEGRATION OF DIPOLES

We have slightly extended the approach outlined in Appendix A of Ref. [10] in order to handle the presence of gluons in the initial state. We refer the reader to Ref. [10] and the original papers CS [13] and CDST [14] for further explanation of the method and notation.

1. Initial-state emitter with initial state spectator

As explained in Ref. [10], we have generalized the dipole phase space (CS, Eq. (5.151)) by introducing a constraint enforced by the factor $\Theta(\alpha - \tilde{v}_i)$. The variable \tilde{v}_i is the rescaled value of the propagator defined by,

$$\tilde{v}_i = \frac{p_a p_i}{p_a p_b} \quad (\text{A1})$$

where p_a is the initial state emitter, p_i is the emitted parton and p_b is the other initial state parton which is the spectator. Further details are given in section 5.5 of CS. In this appendix we extend the previous treatment by considering the remaining q, g and g, g cases. The dipole integrands which we subtract are obtained by modifying CS, Eq. (5.154):

$$\langle \mathbf{V}^{q_a q_i, b}(x_{i,ab}) \rangle = 8\pi\mu^{2\epsilon}\alpha_s C_F \left[\frac{1 + (1 - x_{i,ab})^2}{x_{i,ab}} - \eta \epsilon x_{i,ab} \right] \delta_{ss'} , \quad (\text{A2})$$

$$\langle \mathbf{V}^{g_a g_i, b}(x_{i,ab}) \rangle = 8\pi\mu^{2\epsilon}\alpha_s 2C_A \left[\frac{x_{i,ab}}{1 - x_{i,ab}} + \frac{1 - x_{i,ab}}{x_{i,ab}} + x_{i,ab}(1 - x_{i,ab}) \right] . \quad (\text{A3})$$

We find that the result for the q, g case is given by,

$$\begin{aligned} \tilde{\mathcal{V}}^{q,g}(x; \epsilon, \alpha) &= C_F \left\{ \frac{(1 + (1 - x)^2)}{x} \right. \\ &\times \left[2 \ln(1 - x) - \frac{1}{\epsilon} + \Theta(1 - x - \alpha) \ln \left(\frac{\alpha}{1 - x} \right) \right] + \eta x \left. \right\} + \mathcal{O}(\epsilon) , \end{aligned} \quad (\text{A4})$$

and for the g, g case it is,

$$\begin{aligned} \tilde{\mathcal{V}}^{g,g}(x; \epsilon, \alpha) &= C_A \left\{ \left(\frac{1}{\epsilon^2} - \frac{\pi^2}{6} \right) \delta(1 - x) \right. \\ &+ 2 \left(x(1 - x) + \frac{1 - x}{x} - 1 \right) \left(2 \ln(1 - x) - \frac{1}{\epsilon} \right) \\ &+ \Theta(1 - x - \alpha) \frac{2(x(1 - x) - 1)^2}{x(1 - x)} \ln \left(\frac{\alpha}{1 - x} \right) \\ &\left. - \frac{2}{\epsilon} \frac{1}{[1 - x]_+} + 4 \left[\frac{\ln(1 - x)}{1 - x} \right]_+ \right\} + \mathcal{O}(\epsilon) . \end{aligned} \quad (\text{A5})$$

In the limit $\alpha = 1$ these functions correspond to those given in CS, Eq. (5.155) and also agree with the results of Nagy [34, 35].

2. Initial-state emitter with final-state spectator

In this category, we complete the treatment of Ref. [10] by considering the remaining three cases:

- a) Initial $g \rightarrow q + \bar{q}$,
 - b) Initial $q \rightarrow g + q$,
 - c) Initial $g \rightarrow g + g$,
- (A6)

where the first parton on the right-hand side is an initial-state emitter and the last one is a massive final-state spectator. The phase space is the generalization of CDST, Eq. (5.79) with an extra factor of $\Theta(\alpha - z_i)$.

For case (a) the dipole integrand is given by a generalization of CDST, Eq. (5.82). The result is written in the terms of the variable z_+ defined by,

$$z_+ = \frac{1-x}{1-x+\mu_Q^2}, \quad (\text{A7})$$

and we find,

$$I^{gq}(x; \epsilon, \alpha) = T_R \left\{ \left(x^2 + (1-x)^2 \right) \times \left[\ln \left(\frac{(1-x)^2}{1-x+x\tilde{\mu}^2} \right) - \frac{1}{\epsilon} - \Theta(z_+ - \alpha) \ln \left(\frac{z_+}{\alpha} \right) \right] + 2\eta x(1-x) \right\} + \text{O}(\epsilon). \quad (\text{A8})$$

In this expression we have also introduced the variable,

$$\tilde{\mu}^2 = \frac{\mu^2}{x} = \frac{m^2}{2\tilde{p}_{ai}\tilde{p}_j}, \quad (\text{A9})$$

which only depends on \tilde{p}_{ai} and \tilde{p}_j (defined in CDST Eq. (5.73)), the momenta held fixed when the x integration is performed.

For case (b) the integrand is obtained by generalizing Eq. (5.84) of CDST. Performing the integrals yields the result,

$$I_Q^{qq}(x; \epsilon, \alpha) = C_F \left\{ \frac{(1+(1-x)^2)}{x} \times \left[\ln \left(\frac{(1-x)^2}{1-x+x\tilde{\mu}^2} \right) - \frac{1}{\epsilon} - \Theta(z_+ - \alpha) \ln \left(\frac{z_+}{\alpha} \right) \right] + 2\tilde{\mu}^2 \ln \left(\frac{x\tilde{\mu}^2}{1-x+x\tilde{\mu}^2} \right) - \Theta(z_+ - \alpha) 2\tilde{\mu}^2 \ln \left(\frac{1-z_+}{1-\alpha} \right) \right\} + \eta x \quad (\text{A10})$$

Lastly, the dipole integrand for case (c) is an extension of CDST, Eq. (5.86). The result in this case is,

$$\begin{aligned}
I_Q^{gg}(x; \epsilon, \alpha) = & C_A \left\{ \delta(1-x) \left[\frac{1}{\epsilon^2} + \frac{1}{\epsilon} \ln(1 + \tilde{\mu}^2) + \frac{\pi^2}{6} \right. \right. \\
& + \left. \left. 2 \text{Li}_2(-\tilde{\mu}^2) + 2 \ln(\tilde{\mu}^2) \ln(1 + \tilde{\mu}^2) - \frac{1}{2} \ln^2(1 + \tilde{\mu}^2) \right] \right. \\
& - \frac{1}{\epsilon} \frac{2}{[1-x]_+} - 2 \frac{\ln(1 + \tilde{\mu}^2)}{[1-x]_+} + 4 \left[\frac{\ln(1-x)}{(1-x)} \right]_+ \\
& + 2 \left(x(1-x) + \frac{1-x}{x} - 1 \right) \left[-\frac{1}{\epsilon} + \ln \left(\frac{(1-x)^2}{1-x+x\tilde{\mu}^2} \right) - \Theta(z_+ - \alpha) \ln \left(\frac{z_+}{\alpha} \right) \right] \\
& - \Theta(z_+ - \alpha) \left[2\tilde{\mu}^2 \ln \left(\frac{1-z_+}{1-\alpha} \right) - \frac{2}{(1-x)} \ln \left(\frac{\alpha(1-x+z_+)}{z_+(1-x+\alpha)} \right) \right] \\
& \left. + 2\tilde{\mu}^2 \ln \left(\frac{x\tilde{\mu}^2}{1-x+x\tilde{\mu}^2} \right) - \frac{2}{(1-x)} \ln \left(\frac{2-x+x\tilde{\mu}^2}{1+\tilde{\mu}^2} \right) \right\}. \tag{A11}
\end{aligned}$$

APPENDIX B: THE VIRTUAL $++$ AMPLITUDE

We remind the reader that we calculate the virtual amplitudes for the production of a W that decays leptonically in association with an on-shell top quark,

$$b + g \longrightarrow W(\rightarrow e + n) + t, \tag{B1}$$

where n represents the neutrino, $t^2 = m_t^2$ and $b^2 = g^2 = e^2 = n^2 = 0$.

We first introduce the following short-hand notation,

$$\begin{aligned}
\tau_{xy} &= 2x \cdot y, \quad t_{xy} = (x+y)^2, \quad Q = q^2 = 2e \cdot n \\
q_{xy} &= Q - t_{xy}, \quad \hat{Q} = Q - m_t^2 \\
\delta_{tb} &= \langle b t_0 \rangle [t_0 b] = 2b \cdot t_0 = 2b \cdot t - m_t^2 \frac{b \cdot g}{t \cdot g}, \tag{B2}
\end{aligned}$$

such that the massive top quark momentum t does not appear directly in the following formulae but is instead replaced by the massless vector t_0 , which is suitable for our spinor approach.

Next we define a set of functions that are useful for decomposing the form of the virtual amplitudes. In these formulae, the scalar n -point functions are written using the following

definition,

$$I_0^n(\{p_{1\dots n-1}\}; \{m_{1\dots n}^2\}) = \frac{\mu^{2\epsilon}}{r_\Gamma} \int \frac{d^{4-2\epsilon}l}{(2\pi)^{4-2\epsilon}} \frac{1}{(l^2 - m_1^2)((l - p_1)^2 - m_2^2) \dots ((l - p_{n-1})^2 - m_n^2)}, \quad (\text{B3})$$

where,

$$r_\Gamma = \left(\frac{4\pi\mu^2}{m_t^2} \right)^\epsilon \frac{i}{16\pi^2\Gamma(1-\epsilon)}. \quad (\text{B4})$$

We subsequently identify $I_0^2(\dots) \equiv B_0(\dots)$, $I_0^3(\dots) \equiv C_0(\dots)$ and $I_0^4(\dots) \equiv D_0(\dots)$. The simplest functions contain only bubble integrals,

$$\begin{aligned} l_Q &= 1/\epsilon + 2 - B_0(q; 0, m_t^2) = \hat{Q} \log(-\hat{Q}/m_t^2)/Q \\ l_{tg} &= 1/\epsilon + 2 - B_0(t + g; 0, m_t^2) = \tau_{tg} \log(-\tau_{tg}/m_t^2)/t_{tg} \\ l_{tb} &= 1/\epsilon + 2 - B_0(t + b; 0, m_t^2) = \tau_{tb} \log(-\tau_{tb}/m_t^2)/t_{tb} \\ l_Q^1 &= Q(l_{tg} - l_Q)/q_{tg} \\ l_{tb}^1 &= t_{tb}(l_{tb} - l_Q)/q_{tb} \\ l_{tg}^2 &= (l_{tg} - l_Q)Q^2/q_{tg}^2 + l_Q Q^2/q_{tg}/\tau_{tg} - l_Q Q/q_{tg} + Q/q_{tg} \end{aligned} \quad (\text{B5})$$

Three triangle functions appear in our results, which we choose to keep as independent functions,

$$\begin{aligned} C_0^A &= C_0(t + b, g; 0, m_t^2, m_t^2) \\ C_0^B &= C_0(t, g; 0, m_t^2, m_t^2) \\ C_0^C &= C_0(g + b, t; 0, 0, m_t^2) \end{aligned} \quad (\text{B6})$$

Lastly, we form functions which are combinations of the triangle functions and the basic box integrals that enter our calculation,

$$\begin{aligned} L_1^6 &= \tau_{tb} \tau_{gb} (D_0(g, b, t; 0, 0, 0, m_t^2) - C_0(g, b; 0, 0, 0)/\tau_{tb} \\ &\quad + C_0(g, t + b; 0, 0, m_t^2) (\tau_{gb} + \tau_{tg})/\tau_{gb}/\tau_{tb} - C_0(b, t; 0, 0, m_t^2)/\tau_{gb} \\ &\quad + C_0(g + b, t; 0, 0, m_t^2) (\tau_{tb} (\tau_{tg} + \tau_{tb}) - 2m_t^2 \tau_{gb})/\tau_{gb}/\tau_{tb}^2), \end{aligned} \quad (\text{B7})$$

$$\begin{aligned} L_2^6 &= \tau_{tb} \tau_{tg} (D_0(b, t, g; 0, 0, m_t^2, m_t^2) - C_0(b, t; 0, 0, m_t^2)/\tau_{tg} \\ &\quad + C_0(b, t + g; 0, 0, m_t^2) (\tau_{gb} + \tau_{tb})/\tau_{tg}/\tau_{tb} + C_0(t, g; 0, 0, m_t^2, m_t^2) (2m_t^2 \tau_{gb} - \tau_{tg} \tau_{tb})/\tau_{tg}/\tau_{tb}^2 \\ &\quad + C_0(t + b, g; 0, 0, m_t^2, m_t^2) (\tau_{tg} + \tau_{gb}) (\tau_{tg} \tau_{tb} - 2m_t^2 \tau_{gb})/\tau_{tg}^2/\tau_{tb}^2), \end{aligned} \quad (\text{B8})$$

$$\begin{aligned}
L_3^6 &= \tau_{tg} \tau_{gb} (D_0(b, g, t; 0, 0, 0, m_t^2) - C_0(b, g; 0, 0, 0)/\tau_{tg}) \\
&\quad + C_0(b, t + g; 0, 0, m_t^2) (\tau_{gb} + \tau_{tb})/\tau_{gb}/\tau_{tg} - C_0(g, t; 0, 0, m_t^2)/\tau_{gb} \\
&\quad + C_0(g + b, t; 0, 0, m_t^2) (\tau_{tg} (\tau_{tg} + \tau_{tb}) - 2 m_t^2 \tau_{gb})/\tau_{gb}/\tau_{tg}^2.
\end{aligned} \tag{B9}$$

All the basic scalar integrals, B_0 , C_0 and D_0 are well known [36, 37].

To renormalize the virtual amplitudes we have used the modification of the \overline{MS} scheme in which the top quark is decoupled. The top self-energy is renormalized on-shell so that we have evaluated the self energy in the top-right diagram of Fig. 2 including the following mass counterterm,

$$\delta Z_{mass,c.t.} = -\frac{\alpha_s}{4\pi} \left(\frac{4\pi\mu^2}{m_t^2} \right)^\epsilon \frac{C_F m_t}{\Gamma(1-\epsilon)} \left(\frac{3}{\epsilon} + 5 - \eta \right) \bar{\psi}_t \psi_t, \tag{B10}$$

and we renormalize the top wave function by adding,

$$\frac{\delta Z_{wf}}{2} = -\frac{\alpha_s}{4\pi} \left(\frac{4\pi\mu^2}{m_t^2} \right)^\epsilon \frac{C_F}{2\Gamma(1-\epsilon)} \left(\frac{3}{\epsilon} + 5 - \eta \right) A_{Tree\ Level}. \tag{B11}$$

In the above formulae η is a parameter that specifies the regularization scheme adopted throughout the calculation. $\eta = 0$ corresponds to the 4-dimensional helicity scheme, which we use here, whilst $\eta = 1$ is appropriate in the 't Hooft Veltman scheme. Subtracting the top loop contribution to the gluon self energy at zero momentum transfer enables the coupling constant to evolve due to the presence of 5 light flavours only. Finally, the partial cancellation of the coupling constant renormalization and this top contribution to the gluon self energy give us the last contribution,

$$\delta Z'_g = -\frac{\alpha_s}{4\pi} (4\pi)^\epsilon \frac{(11N/6 - 2T_R n_f/3)}{\epsilon\Gamma(1-\epsilon)} A_{Tree\ Level}. \tag{B12}$$

We are now in a position to write down the amplitudes for the specific helicity choice ‘++’. The first ‘+’ signifies the helicity of the gluon and the second ‘+’ the spin of the top quark in a basis determined by our decomposition in Eq. (B2). The tree-level amplitude is,

$$A_{Tree\ Level}^{++} = \frac{\sqrt{2} g_s g_W^2 T^a}{W_{prop}^-} A_0^{++}, \tag{B13}$$

where,

$$A_0^{++} = -m_t \frac{\langle g e \rangle}{\langle g b \rangle \langle g t_0 \rangle^2} (\langle b t_0 \rangle [b n] + \langle g t_0 \rangle [g n]), \tag{B14}$$

and,

$$W_{prop}^- = q^2 - M_W^2 + iM_W\Gamma_W. \tag{B15}$$

The corresponding virtual amplitude is decomposed into a piece containing poles in ϵ which is proportional to the lowest order result, plus a finite remainder,

$$A_{Virtual}^{++} = \frac{\alpha_s}{4\pi} \frac{\sqrt{2} g_s g_W^2 T^a}{\Gamma(1-\epsilon) W_{prop}^-} \left(\frac{4\pi\mu^2}{m_t^2} \right)^\epsilon [(F + P_{wf}) \cdot A_0^{++} + A_1^{++}]. \quad (B16)$$

The pole pieces are given by,

$$\begin{aligned} F = & -N (3/2/\epsilon^2 - 1/\epsilon \log(-\tau_{tg}/m_t^2) - 1/\epsilon \log(-\tau_{gb}/m_t^2) \\ & + 1/2/\epsilon + \log(-\tau_{tg}/m_t^2)^2 + 1/2 \log(-\tau_{gb}/m_t^2)^2) \\ & + 1/2/N (1/\epsilon^2 - 2/\epsilon \log(-\tau_{tb}/m_t^2) + 1/\epsilon + 2 \log(-\tau_{tb}/m_t^2)^2) \\ & - N (\text{Li}_2(t_{tg}/m_t^2) + \pi/12) + (\text{Li}_2(t_{tb}/m_t^2) + \pi^2/12)/N, \end{aligned} \quad (B17)$$

while the term which is the sum of coupling constant and wave-function renormalization is,

$$P_{wf} = (2T_R n_f/3 - 11N/6) (1/\epsilon - \log(\mu^2/m_t^2)) - 3C_F/2 (1/\epsilon + 5/3). \quad (B18)$$

The remainder is then written in terms of our functions as,

$$\begin{aligned} A_1^{++} = & \frac{m_t \langle g e \rangle [g n]}{\langle g b \rangle \langle g t_0 \rangle \langle b t_0 \rangle [b t_0]} \left\{ \frac{1}{N} [L_1^6 \delta_{tb}/2 + L_2^6 (\delta_{tb}/2 - q_{tg} \delta_{tb}/\tau_{gb} - q_{tg} m_t^2/2/\tau_{tg}) \right. \\ & - C_0^A \tau_{gb} \delta_{tb} m_t^2/\tau_{tg} - 2C_0^A \delta_{tb} m_t^2 + 2C_0^B \delta_{tb} m_t^2 + C_0^C \tau_{gb} \delta_{tb} m_t^2/\tau_{tb} + l_{tb}^1 \tau_{gb} t_{tb}/\tau_{tg} + l_Q \delta_{tb} \\ & - l_{tg} t_{tg} \delta_{tb}/\tau_{tg} - l_{tb} t_{tb} \tau_{tb}/\tau_{tg} + l_{tb} \tau_{gb} \delta_{tb}/\tau_{tb} + l_Q \tau_{tb} t_{tb}/\tau_{tg}] + C_F [l_{tg} q_{tb} t_{tg}/\tau_{tg} - l_{tg} Q - \delta_{tb} \\ & + l_{tg} \delta_{tb} + 2 l_{tg} t_{tg} \delta_{tb}/\tau_{tg} + q_{tg} \delta_{tb}/\tau_{tg} - 2 \delta_{tb} \hat{Q}/\tau_{tg}] + N [-L_3^6 \delta_{tb}/2 - C_0^C \tau_{gb} \delta_{tb} m_t^2/\tau_{tg}] \left. \right\} \\ & + \frac{m_t \langle g e \rangle [b n]}{\langle g b \rangle \langle g t_0 \rangle^2 [b t_0]} \left\{ \frac{1}{N} [L_1^6 \tau_{tb}/2 + L_2^6 (\delta_{tb} - t_{tb}/2 + \tau_{tb} \tau_{tg}/\tau_{gb}) + 2C_0^A q_{tb} \tau_{gb} \delta_{tb} m_t^2/\tau_{tb}/\tau_{tg} \right. \\ & + C_0^A q_{tb} \delta_{tb} m_t^2/\tau_{tb} - C_0^B q_{tb} \delta_{tb} m_t^2/\tau_{tb} - C_0^B \tau_{gb} \delta_{tb} m_t^2/\tau_{tb} - 2C_0^C \tau_{gb} \delta_{tb} m_t^2/\tau_{tg} - l_{tb} \tau_{tg} \delta_{tb}/\tau_{tb} \\ & - l_{tg} \delta_{tb}] + C_F [-4C_0^C \tau_{gb} \delta_{tb} m_t^2/\tau_{tg} + 2l_Q^1 \tau_{gb} Q/\tau_{tg} + l_Q^1 \tau_{gb} - 2l_{tg} q_{tb} - 2l_{tg} q_{tb} Q/\tau_{tg} \\ & + l_{tg} \tau_{tg} Q/t_{tg} + l_Q q_{tg} q_{tb}/\tau_{tg} + l_Q Q q_{tb}/\tau_{tg} + l_Q q_{tb} + l_Q Q - q_{tg} \tau_{tg}/t_{tg} + \tau_{gb} - \delta_{tb}] \\ & \left. + N [L_3^6 \tau_{tb}/2 - L_3^6 \delta_{tb}] \right\} \\ & + \frac{m_t \langle b e \rangle [b n]}{\langle g b \rangle \langle g t_0 \rangle \langle b t_0 \rangle [b t_0]} \left\{ \frac{1}{N} [-L_2^6 q_{tb} m_t^2/2/\tau_{tg} + C_0^A q_{tb}^2 \delta_{tb} m_t^2/\tau_{tb}/\tau_{tg} - C_0^B q_{tb} \delta_{tb} m_t^2/\tau_{tb} \right. \\ & - l_Q^1 \tau_{gb} Q/\tau_{tg} + l_{tb} Q \delta_{tb}/\tau_{tb} - l_Q Q q_{tb}/\tau_{tg} + l_{tg} q_{tb} Q/\tau_{tg}] + C_F [l_{tg}^2 \tau_{gb}^2/\tau_{tg} + 2l_Q^1 \tau_{gb}^2 Q/\tau_{tg}^2 \\ & - 3l_Q^1 \tau_{gb}^2/\tau_{tg} - 2l_Q^1 \tau_{gb} + 4l_{tg} q_{tb} Q/\tau_{tg} - 2l_{tg} q_{tb}^2 Q/\tau_{tg}^2 - 2l_{tg} t_{tg} q_{tb}^2/\tau_{tg}^2 + 2l_{tg} q_{tb}^2/\tau_{tg} \\ & - l_{tg} \tau_{tg} Q/t_{tg} + l_Q q_{tg} q_{tb}^2 m_t^2/\tau_{tg}^2/\hat{Q} + l_Q Q q_{tg} q_{tb}^2/\tau_{tg}^2/\hat{Q} - 2l_Q Q q_{tb}/\tau_{tg} + l_Q q_{tb}^2 m_t^2/\tau_{tg}/\hat{Q} \\ & \left. + l_Q Q q_{tb}^2/\hat{Q}/\tau_{tg} - q_{tb} \delta_{tb}/\tau_{tg} - q_{tb}^2/\tau_{tg} + \tau_{tg} Q/t_{tg}] \right\}. \end{aligned} \quad (B19)$$

The expressions for the other amplitudes are similar but slightly longer, requiring the addition of a further 5 functions to describe them compactly. We do not reproduce them here, but they are available as Fortran files from the authors on request.

-
- [1] G. Altarelli and M. L. Mangano (editors), “Standard model physics (and more) at the LHC”, Geneva, Switzerland, October 14-15, 1999.
 - [2] J. M. Campbell and R. K. Ellis, Phys. Rev. D **60**, 113006 (1999) [arXiv:hep-ph/9905386].
 - [3] J. M. Campbell and R. K. Ellis, Phys. Rev. D **62**, 114012 (2000) [arXiv:hep-ph/0006304].
 - [4] J. Campbell and R. K. Ellis, Phys. Rev. D **65**, 113007 (2002) [arXiv:hep-ph/0202176].
 - [5] A. S. Belyaev, E. E. Boos and L. V. Dudko, Phys. Rev. D **59**, 075001 (1999) [arXiv:hep-ph/9806332].
 - [6] T. M. P. Tait, Phys. Rev. D **61**, 034001 (2000) [arXiv:hep-ph/9909352].
 - [7] A. Belyaev and E. Boos, Phys. Rev. D **63**, 034012 (2001) [arXiv:hep-ph/0003260].
 - [8] W. T. Giele, S. Keller and E. Laenen, Phys. Lett. B **372**, 141 (1996) [arXiv:hep-ph/9511449].
 - [9] S. Zhu, Phys. Lett. B **524**, 283 (2002) [Erratum-ibid. B **537**, 351 (2002)].
 - [10] J. Campbell, R. K. Ellis and F. Tramontano, Phys. Rev. D **70**, 094012 (2004) [arXiv:hep-ph/0408158].
 - [11] R. K. Ellis, D. A. Ross and A. E. Terrano, Nucl. Phys. B **178** (1981) 421.
 - [12] S. Catani and M. H. Seymour, Phys. Lett. B **378** (1996) 287 [hep-ph/9602277].
 - [13] S. Catani and M. H. Seymour, Nucl. Phys. B **485** (1997) 291 [Erratum-ibid. B **510** (1997) 291] [hep-ph/9605323].
 - [14] S. Catani, S. Dittmaier, M. H. Seymour and Z. Trocsanyi, Nucl. Phys. B **627**, 189 (2002) [arXiv:hep-ph/0201036].
 - [15] T. Gottschalk, Phys. Rev. D **23**, 56 (1981).
 - [16] C. R. Schmidt, Phys. Rev. D **54**, 3250 (1996) [arXiv:hep-ph/9504434].
 - [17] R. Pittau, Comput. Phys. Commun. **111**, 48 (1998) [arXiv:hep-ph/9712418].
 - [18] J. M. Campbell, E. W. N. Glover and D. J. Miller, Nucl. Phys. B **498**, 397 (1997) [arXiv:hep-ph/9612413].
 - [19] E. Boos and T. Plehn, Phys. Rev. D **69**, 094005 (2004) [arXiv:hep-ph/0304034].
 - [20] P. Nason, S. Dawson and R. K. Ellis, Nucl. Phys. B **303** (1988) 607.

- [21] N. Kauer and D. Zeppenfeld, Phys. Rev. D **65**, 014021 (2002) [arXiv:hep-ph/0107181].
- [22] H. L. Lai *et al.* [CTEQ Collaboration], Eur. Phys. J. C **12**, 375 (2000) [arXiv:hep-ph/9903282].
- [23] F. Maltoni and T. Stelzer, JHEP **0302**, 027 (2003) [arXiv:hep-ph/0208156].
- [24] P. Azzi *et al.* [CDF Collaborattion], arXiv:hep-ex/0404010.
- [25] J. Pumplin, D. R. Stump, J. Huston, H. L. Lai, P. Nadolsky and W. K. Tung, JHEP **0207**, 012 (2002) [arXiv:hep-ph/0201195].
- [26] A. D. Martin, R. G. Roberts, W. J. Stirling and R. S. Thorne, Eur. Phys. J. C **28**, 455 (2003) [arXiv:hep-ph/0211080].
- [27] M. Dittmar and H. K. Dreiner, Phys. Rev. D **55**, 167 (1997) [arXiv:hep-ph/9608317].
- [28] T. Binoth, M. Ciccolini, N. Kauer and M. Kramer, arXiv:hep-ph/0503094.
- [29] M. Duhrssen, K. Jakobs, P. Marquard and J. J. van der Bij, arXiv:hep-ph/0504006.
- [30] ATLAS Detector and Physics Performance TDR, The ATLAS Collaboration (CERN/LHCC/99-14).
- [31] G. Davatz, G. Dissertori, M. Dittmar, M. Grazzini and F. Pauss, JHEP **0405**, 009 (2004) [arXiv:hep-ph/0402218].
- [32] T. Sjostrand, P. Eden, C. Friberg, L. Lonnblad, G. Miu, S. Mrenna and E. Norrbin, Comput. Phys. Commun. **135**, 238 (2001) [arXiv:hep-ph/0010017].
- [33] C. A. Nelson, Phys. Rev. D **37**, 1220 (1988).
- [34] Z. Nagy and Z. Trocsanyi, Phys. Rev. D **59**, 014020 (1999) [Erratum-ibid. D **62**, 099902 (2000)] [arXiv:hep-ph/9806317].
- [35] Z. Nagy, Phys. Rev. D **68**, 094002 (2003) [arXiv:hep-ph/0307268].
- [36] G. 't Hooft and M. J. G. Veltman, Nucl. Phys. B **153**, 365 (1979).
- [37] W. Beenakker, S. Dittmaier, M. Kramer, B. Plumper, M. Spira and P. M. Zerwas, Nucl. Phys. B **653** (2003) 151 [arXiv:hep-ph/0211352].
- [38] At the Tevatron, this is due to the fact that the machine is a proton anti-proton collider. At the LHC, the equality is because the perturbatively-derived bottom quark distribution functions that we use are the same for \bar{b} and b quarks.
- [39] This can be seen by examining a study of the similar process, charged Higgs production in association with a top quark [19]. We have also reproduced this result for the process at hand.
- [40] A NLO calculation including the decays of the top quarks is not currently available. However one could, for instance, use a lowest order calculation including the decays and normalize to

the inclusive $t\bar{t}$ NLO rate, which is known [20].

- [41] As we have already pointed out, interference effects between singly- and doubly-resonant diagrams are small. Although this procedure is not strictly gauge invariant, it is no more serious an error than that incurred when introducing a Breit-Wigner width for resonant propagators.
- [42] We use CTEQ5L1 for the lowest order calculation and CTEQ5M1 at NLO, the versions that include the improved evolution code.